Journal of Structural Geology 31 (2009) 972–988

Contents lists available at ScienceDirect

Journal of Structural Geology

journal homepage: www.elsevier.com/locate/jsg

Energy budget during fold tightening of a multilayer fold

Zeshan Ismat*

Department of Earth and Environment, Franklin and Marshall College, Lancaster, PA 17604-3003, United States

ARTICLE INFO

Article history:
Received 13 March 2007
Received in revised form
9 July 2008
Accepted 16 October 2008
Available online 29 October 2008

Keywords:
Folding
Multilayer
Energy consumption
Work
Cataclastic flow

ABSTRACT

The Canyon Range syncline, Central Utah, is composed of an alternating sequence of competent quartzite and incompetent argillite layers and is used here as a natural case study of multilayer folding processes. Geometric details of this fold are evaluated in terms of energy consumption in order to determine which kinematic components of folding are dominant at various stages of fold tightening. In addition, this paper attempts to evaluate what mechanism(s) (e.g. kink folding, fracture formation and sliding along surfaces) are involved in each kinematic component.

In general, the patterns preserved in the Canyon Range syncline are comparable to multilayer folding models. In more detail, the following is concluded from this case study. (1) The *competent* and *incompetent* members deformed primarily by cataclastic flow and consumed approximately equal amounts of energy. (2) The roles of original competent and incompetent layers reversed during folding. (3) As the syncline tightened, less energy was consumed with *increasing* hinge fractions. (4) The least amount of energy was consumed with 40° limb dips (i.e., 100° interlimb angle). (5) With an open fold geometry (interlimb angle $\geq$140°), the hinge region consumed ~70% of the fold's total energy. (6) Once the fold reached an interlimb angle of ~60°, the limbs consume close to 70% of the total energy. (7) When the fold reached an interlimb angle of $\leq$60°, the *incompetent* layer(s) consumed ~90% of the fold's energy.

1. Introduction

The Canyon Range syncline, Central Utah, is a well understood multilayer fold composed of an alternating sequence of *competent* and *incompetent* layers. Different stages of the syncline's folding history have been tracked on the basis of detailed geometric analyses. The Canyon Range syncline is re-examined here in terms of energy consumption in order to provide more detailed constraints to the fold's geometry for various stages of its deformation history (Mitra and Boyer, 1986; Masek and Duncan, 1998; Cooke and Murphy, 2004). The syncline's geometry is used to evaluate the relative competencies of the folded layers at various stages of fold tightening. The amount of energy consumed by a fold during its formation is a function of the relative competencies of the layers and the processes involved in folding.

Bayly (1974) was one of the earliest geologists to examine the development of (theoretical) multilayer folds in terms of energy consumption. This paper applies the approach of Bayly (1974) to a *natural* multilayer fold; his seminal work is focused on for two main reasons. First, the equations he developed to estimate energy consumption are based on fold geometry. Therefore, these equations are applicable to most folds formed under a wide range of deformation conditions. Second, the equations are very flexible; different values for limb dips (interlimb angle), bed thickness, competency contrast, hinge fraction, etc. can be assigned for each stage of folding.

Similar to Bayly (1974), the Canyon Range syncline is partitioned into four sub-regions, which are used to define five major kinematic components of folding: limb shear, limb thickening/thinning, hinge shear, hinge thickening/thinning, and hinge curvature (Fig. 1a). These kinematic components are tracked in order to document where folding energy is expended at different stages of fold tightening (Fig. 1a and b). This analysis provides information on the relative competencies of the folded layers, which ultimately influence the fold shape. The activity/inactivity of the five kinematic components controls the resulting fold geometry; these results are compared to existing multilayer folding models.

The goals of this paper are the following. (1) Determine how much total energy is consumed by the Canyon Range syncline during fold tightening and assess how a variety of mechanisms (e.g. kink folding, fracture formation and sliding along surfaces) contribute to this total value. (2) Determine which kinematic components are used at various stages of fold tightening and, more specifically. (3) How the competent and incompetent layers contribute to these five kinematic components.

* Tel.: +1 1717 358 4485; fax: +1 1717 291 4186.
E-mail address: zeshan.ismat@fandm.edu

0191-8141/$ – see front matter © 2008 Elsevier Ltd. All rights reserved.
doi:10.1016/j.jsg.2008.10.006

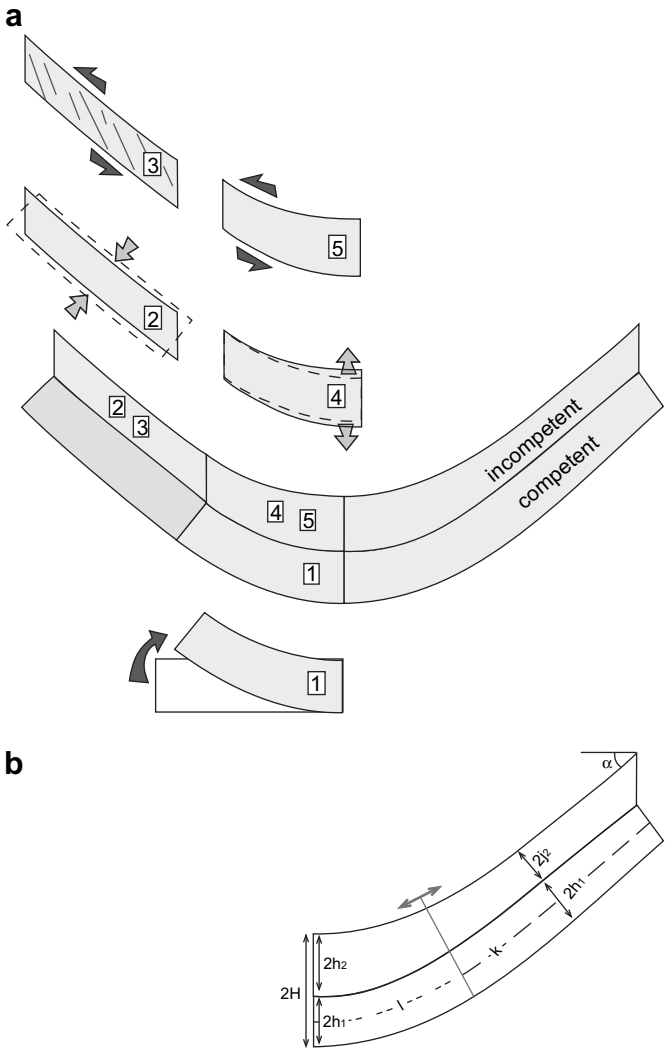

Fig. 1. (a) Two dimensional model of an upright, symmetrical multilayer fold illustrating five kinematic components of folding: (1) competent hinge curvature, (2) incompetent limb thickening/thinning, (3) incompetent limb layer-parallel shear, (4) incompetent hinge thickening/thinning, and (5) incompetent hinge layer-parallel shear (adapted from (Bayly 1974)). (b) (see Appendix) Variables used to construct multilayer fold model. α is the limb dip. l is the median length of the hinge region and k is the median length of the limb; both are measured along the center line within the competent member. Solid gray line with double headed arrow separates the limb region from the hinge region, and can be adjusted depending upon fold geometry. $l/(l+k)$ defines the hinge fraction. $2h_1$ is the thickness of the competent member, and is assumed to be constant throughout the fold. $2h_2$ is the thickness of the incompetent hinge. $2j_2$ is the average thickness of the incompetent limb, and is measured at the mid-point of the limb's median length (mid-point of length k).

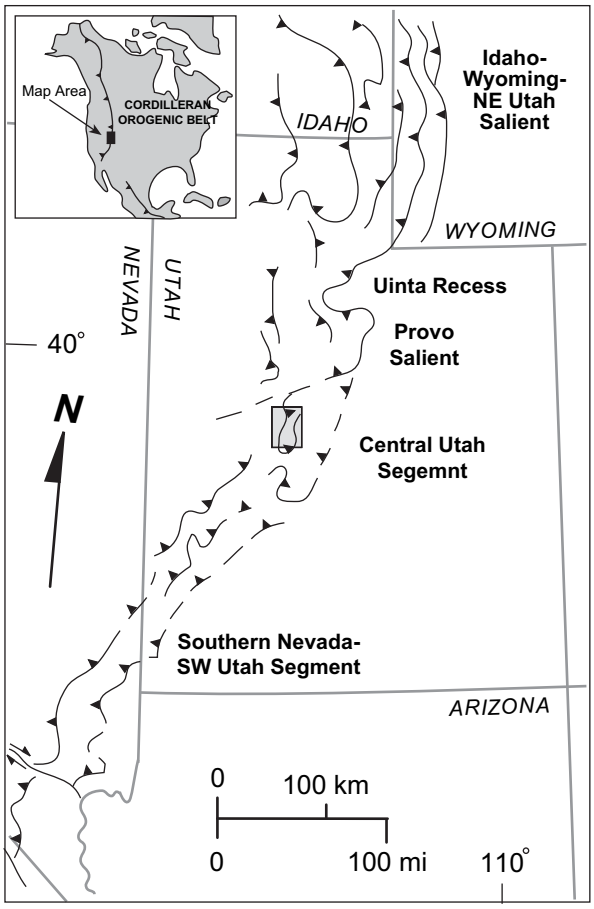

Fig. 2. Southern portion of the Sevier FTB. Boxed area is enlarged in Fig. 3.

2. Natural case study

2.1. Overview

The Canyon Range (CR) syncline, part of the folded CR thrust sheet of the Sevier fold-thrust belt, is used as a natural case study (Figs. 2 and 3). More specifically, this analysis focuses on the *core* of the CR syncline (Fig. 3a), which is defined by the Pioche Formation, a unit made up of interbedded quartzites and argillites (Fig. 3b).

Cores of folds hold critical clues to the evolution of a folded region because structures that accommodate space problems are typically localized there. Based on the CR syncline, the following questions regarding fold tightening are addressed in terms of energy consumption. (1) What are the roles of the *competent* and *incompetent* layers and how, when and where do they interact with each other? Here, competency is described as the 'degree of ductility' (Treagus, 1988, 1993). The shape (i.e., fold class) of the folded layers can geometrically illustrate the degree of ductility (Ramsay, 1974). (2) How does the hinge fraction vary during fold tightening and how it may influence the overall fold shape?

The core of the CR syncline is an ideal fold to study for various reasons. First, this portion of the fold is very well exposed. Second, most of its fold tightening occurred under shallow crustal conditions ($\leq$5 km depth), i.e., within the elastico-frictional regime (Ismat and Benford, 2007). Because the deformation took place at temperatures and pressures lower than greenschist grade, cross-cutting and overprinting relationships are well preserved. In the elastico-frictional regime, deformation takes place primarily by fracturing and cataclastic flow, so the folding history can be unraveled by tracking fracture patterns and other structures preserved in the syncline (Ismat and Mitra, 2005a). Third, the fold is tight (interlimb angle $\sim$52°), so folding behavior can be traced for a wide range of fold geometries (Fig. 3b). Fourth, the core of this syncline is composed of an alternating sequence of competent quartzite and incompetent argillite layers (Fig. 3b). So, this fold can be directly compared to multilayer folding models. Finally, the fold formed under a consistent overall E–W sub-horizontal shortening direction, so folding related complexities are minimized (Ismat and Mitra, 2001a, 2005a,b).

2.2. Structures associated with fold tightening

Conjugate–conjugate fracture sets (Reches, 1978a, 1983) are preserved in the Pioche quartzite and a minimum of two cleavage sets are preserved in the Pioche argillite. Slickenlines preserved on

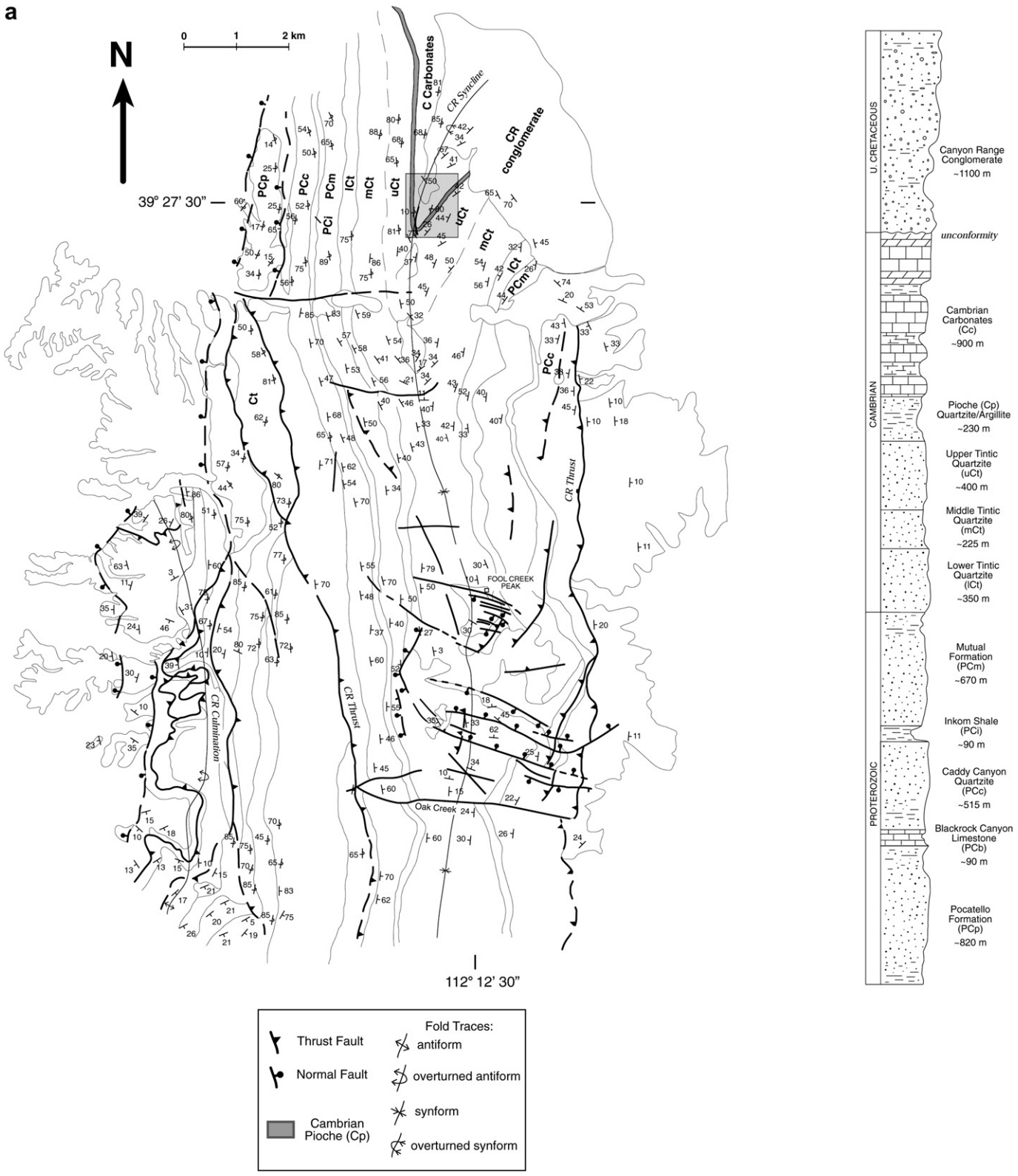

Fig. 3. (a) Geologic map and stratigraphic column of the Canyon Range (CR). The Cambrian Pioche Formation (Cp) is shaded. (b) Enlarged from boxed area in part (a). Down-plunge projection of the Pioche Formation. The argillite layer is shaded light gray and the quartzite layers are shaded dark gray. Box-fold geometry of the Pioche fold is shown as black lines; the length and geometry of this box shape is used in the construction in Fig. 6. Locations of the second-order parasitic folds are shown with white squares. White circle shows location of relict synformal hinge. (c) Equal-Area plot of relict synformal hinge. Great circles illustrate the average bedding orientations of the east and west limbs. The angle between the poles to bedding ($P_{\text{east limb}}$ and $P_{\text{west limb}}$) is 132° and defines its interlimb angle.

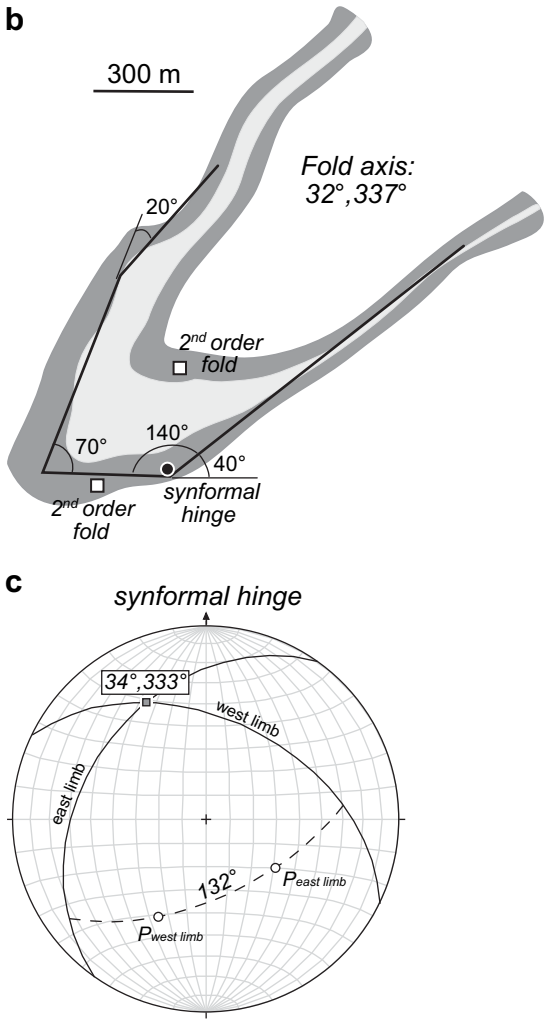

Fig. 3. (*continued*).

the fractures sets result in an average m-pole (i.e., pole to the average motion plane) plunging 10° toward 358°. Detailed bedding and fracture population data collected from asymmetric parasitic folds (10 m scale), which are all found close to the hinge region, plunge ~10° toward 359° (Ismat and Benford, 2007). Both of these have gentler plunges than the overall plunge of the CR syncline (32°, 337°). Because of this, it has been interpreted that the CR syncline had already developed a plunge of ~20° before these structures developed (Lawton et al., 1997; Ismat and Benford, 2007). So, the slickenlines and parasitic folds do not track the CR syncline's entire folding history; they formed during an intermediate or late stage of folding. In addition, because the plunges of the m-pole and the parasitic folds are similar, we can say that they formed at approximately the *same* intermediate or late stage (Ismat and Benford, 2007).

A synformal hinge, much larger than the parasitic folds, is preserved within the east limb of the first-order CR syncline (Fig. 3b and c). This (eastern) hinge plunges 34° toward 333° and has interlimb angle of 132° (Fig. 3c). Earlier work suggests that this synformal hinge is the inactive hinge of an original double-kink box fold, while the current hinge of the first-order CR syncline is the other kink hinge that continued to be active (Ismat and Benford, 2007).

2.3. The role of 'competent' and 'incompetent' layers

The conjugate–conjugate sets of fractures preserved in the Pioche quartzite yield shortening directions that are sub-parallel to bedding in both the limbs and hinge of the fold (Fig. 4); this orientation suggests that the fractures formed when the beds were sub-horizontal, accommodating layer-parallel shortening (LPS) (Fig. 5a and b) (Ismat and Benford, 2007). The four fracture sets, and bedding, define rhomb-shaped blocks, which slid past each other in order to accommodate folding by (block-supported) cataclastic flow. Sliding can take place along surfaces that lie within ~60° of the maximum shortening or extension direction (Donath and Parker, 1964; Paterson, 1978; Twiss and Moores, 1992).

Three-dimensional ductile deformation, such as cataclastic flow, can be accommodated by slip on five independent slip systems (i.e., von Mises criterion) (Paterson, 1978; Twiss and Moores, 1992). These slip systems can include fracture and cleavage surfaces (Mandl, 2000). In natural rocks, this requirement for five independent slip systems is relaxed due to natural heterogeneities (Paterson, 1978). Experimental work on homogeneous deformation of quartzites suggests that the fifth slip system is close to two orders of magnitude less active than the most active slip system and that the fourth slip system is almost one order of magnitude less active (Lister et al., 1978; Paterson, 1978). Previous work in the CR syncline reveals similar results; ductile deformation via (block-supported) cataclastic flow was accommodated by sliding on a minimum of three surfaces (Ismat and Mitra, 2001a; Ismat, 2006).

As the limbs rotated with progressive fold tightening, the conjugate–conjugate fracture sets were passively rotated and later reactivated (via renewed slip) to accommodate thinning and vertical stretching of the limbs, while fractures in the hinge region continued to accommodate shortening and thickening of the beds

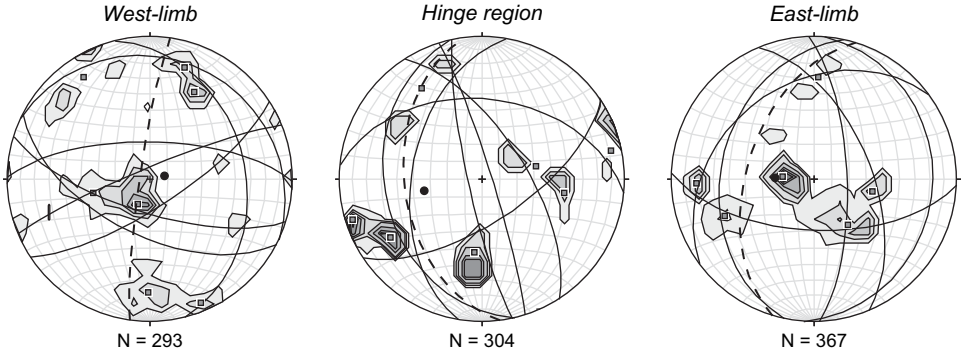

Fig. 4. Fracture networks from the west limb, hinge region and east limb of the Pioche quartzite layers. Fractures were weighted and plotted as poles on Equal Area nets. Average fracture sets, determined from the pole concentrations, are plotted as great circles. The poles to these great circles are shown as gray squares. Shortening/extension directions (black dots) are determined from the acute bisector of the conjugate–conjugate fracture sets. The average bedding orientation is represented as a dashed great circle.

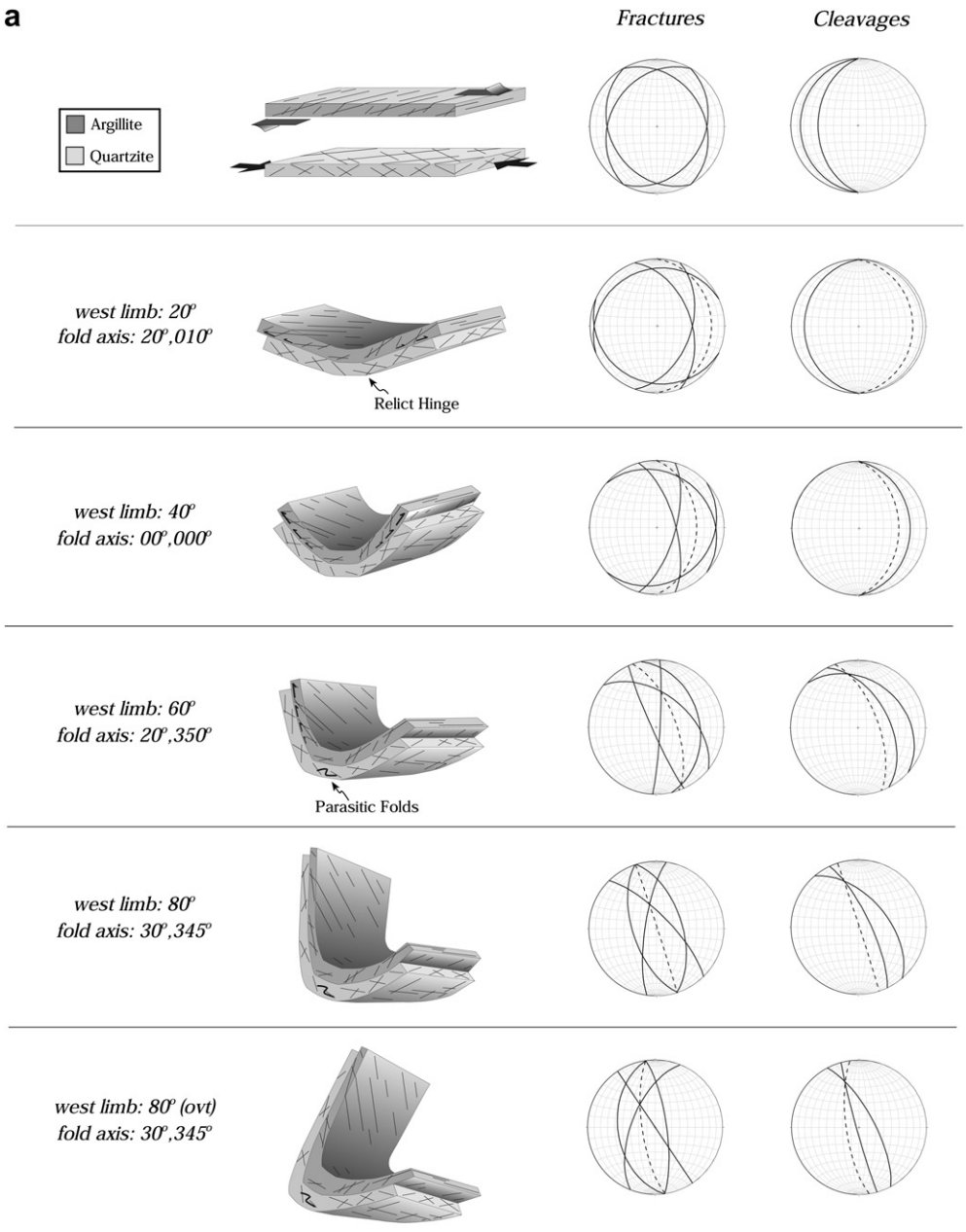

Fig. 5. (a) Kinematic model of the Pioche Formation and associated Equal-Area plots illustrating rotated fracture and cleavage sets (see Table 1). Bedding is shown as a dashed great circle. (b) Graph illustrating number of active surfaces (fractures, cleavages, bedding) in the Pioche quartzite and argillite for different increments of fold tightening, i.e., limb dip (see Table 1). Horizontal dashed lines mark the point below which (block-suported) cataclastic flow cannot be the dominant deformation mechanism.

(Fig. 5a) (Ismat and Benford, 2007). As the fold tightened, the incompetent Pioche argillite deformed and flowed from the limbs to the hinge (Fig. 3b), also by cataclastic flow, as rhomb-shaped blocks defined by two sets of LPS cleavage surfaces plus bedding, slid past one another (Fig. 5a).

After the CR syncline's limbs reached dips of ~40° (interlimb angle of 100°), folding continued by rotation of the west limb (Fig. 5a) (Ismat and Mitra, 2005b). Based on the model illustrated in Fig. 5a and b, at this stage, the number of 'active' fracture sets, i.e., those in positions for reactivation, decreased from 5 to 3, while all three surfaces in the argillite remained in positions for reactivation (Table 1). So, as cataclastic flow in the quartzite became less effective, the role of the argillite unit in the folding process became more prominent.

Once the west limb reached a limb dip of 60° (80° interlimb angle), the fractures and cleavages rotated into positions to accommodate limb thinning and extension. Three surfaces in the quartzite were in positions for reactivation, while only two surfaces were active in the argillite. Therefore, cataclastic flow may not have been the only process responsible for limb rotation at this fold stage; flexural slip may have assisted migration of the incompetent argillite to the hinge region in order to fill a potential gap (i.e., saddle reef) there.

Beyond a limb dip of 80° (interlimb angle ≤60°), the fractures and cleavage surfaces were rotated into positions where a minimum of 4–5 surfaces in the quartzite and all three surfaces in the argillite were reactivated to accommodate vertical limb thinning and stretching (Fig. 5b, Table 1). So, in the later stages of fold tightening (≥80° limb dip), the quartzite and argillite members equally influenced the Pioche fold's geometry, where the competent layer 'softened' and flowed with the incompetent argillite.

Many models predict that once a fold reaches an interlimb angle of ~60° (i.e., limb dips of 60°), the fold 'locks' because the competent limbs can no longer rotate and that beyond this 'locking' point, the incompetent member controls the folding process (Ramsay, 1974; Williams, 1980). The natural case study examined here suggests a slightly different scenario. There does not appear to be a 'locking point', but instead a gradual change between 40° and 60° limb dips (i.e., between 100° and 80° interlimb angles) during which the argillite controlled the fold geometry.

As folding progressed, argillite migrated from the limbs to the hinge; this may have induced the formation of parasitic folds in the hinge region to accommodate excess volume of material there. At the same time, the Pioche quartzite layers moved closer together in the limbs as the argillite moved from the limbs to the hinge. Early LPS fracture sets were reactivated to accommodate vertical limb thinning and extension. This late stage reactivation is evidenced by slickenlines, which are predominantly preserved on those fracture sets within steep beds of the west limb. Because of this concurrent argillite migration and fracture reactivation, the average m-pole and the parasitic folds share similar orientations.

Table 1
Fracture, cleavage and bedding orientation for various stages of fold tightening. *S* and *E* indicate active surfaces that accommodated shortening and extension, respectively. *N* identifies those surfaces that are not in orientations for reactivation.

West-limb dip (°)	Fold axis (plunge,trend)	Bed orientation	Fractures (quartzite)	Cleavages (argillite)
00	00,000	00,000 (S)	30,240 (S) 30,060 (S) 30,300 (S) 30,120 (S)	40,270 (S) 15,270 (S)
20	00,000	20,090 (S)	16,204 (S) 48,070 (S) 16,336 (S) 48,110 (S)	20,270 (S) 05,090 (S)
40	00,000	40,090 (S)	20,138 (S) 67,074 (E) 20,042 (S) 67,106 (E)	00,247 (S) 25,090 (S)
60	20,350	65,070 (E)	36,077 (S) 85,246 (E) 50,039 (N) 85,093 (E)	30,042 (N) 52,063 (S/E)
80	30,345	89,072 (E)	59,073 (E) 61,251 (E) 74,046 (N) 76,278 (E)	55,050 (E) 76,065 (E)
100	30,345	74,262 (E)	76,082 (E) 44,262 (E) 90,236 (E) 61,292 (E)	71,062 (E) 87,255 (E)

2.4. Summary of kinematic history

The kinematic details for folding of the CR syncline are based on the data, analysis and interpretation of the structures preserved in its core, as presented above. The following is a summary of this kinematic history.

1. Early LPS cleavage surfaces formed in the Pioche argillite and LPS conjugate–conjugate fracture sets developed in the Pioche quartzite, both when the Pioche unit was sub-horizontal.
2. Up to limb dips of ~40° (i.e., ~100° interlimb angle), the Pioche unit has a double-kink box-fold geometry. Folding was controlled by (block-supported) cataclastic flow by reactivating the early LPS conjugate–conjugate fracture sets in the quartzite layers.
3. Beyond ~40° limb dips, the western hinge of the double-kink remained active while the eastern hinge was absorbed into the east limb of the first-order CR syncline and is preserved as a relict feature.
4. Between limb dips of ~40° and 60° (i.e., between interlimb angles of 100° and 80°), the incompetent argillite member began to control the folding process. The Pioche argillite flowed from the limbs to the hinge in order to maintain contact between the competent quartzite layers (Donath and Parker, 1964).
5. During argillite migration from the limbs to the hinge, parasitic folds formed in the hinge region, possibly in response to the excess volume there.
6. Beyond a limb dip of ~80° (i.e., interlimb angle of ≤60°), the Pioche quartzite and argillite contributed equally to the fold shape as both deformed by cataclastic flow.

3. General work equations

The five kinematic components of folding (Bayly, 1974) used in this paper perform work in the form of internal deformation within a fold. The mechanisms used to accommodate these five folding components require input of energy, which can be summed to estimate the total work for internal deformation. This internal work value is an estimate of the mechanical work done in producing the observed structure and so gives the minimum amount of energy consumed. Other forms of energy may have been stored elastically and/or were dissipated as heat. Because there is no record for this in the rocks, it is not incorporated into the total internal work equation. In the elastico-frictional regime, the work for internal energy is given by

$$W_t = W_k + W_f + W_s \quad (1)$$

(Elliott, 1976b; Mitra and Boyer, 1986; Ismat and Mitra, 2005a; Cooke and Murphy, 2004), where the total internal work (W_t) is the sum of the work involved in kinking (W_k), the work involved in formation of outcrop-scale fractures and cleavage surfaces (W_f), and the work involved in shearing along outcrop-scale fractures and other surfaces (W_s). The details of these terms are discussed in order. It should be noted that for contractional orogenic belts, the total work required to accommodate deformation in the upper crust by elastico-frictional mechanisms is nearly identical to the amount of work required to accommodate deformation at deeper levels by crystal–plastic deformation mechanisms (Ismat and Mitra, 2005a).

3.1. Kink folding

Fold shapes are represented as kink folds for a simple, first-order calculation. The work involved for kink folding is

$$W_k = \tau_{ib} A 1000 \tan\theta \text{ J}, \quad (2)$$

where τ_{ib} is the interbed shear stress, A is the cross-sectional area of the folded unit, 1000 m is its unit width, and θ is the kink angle (Mitra and Boyer, 1986; Ismat and Mitra, 2005a).

3.2. Fracture and cleavage formation

The estimated work done by fracturing ($W_{f\text{-quartzite}}$) only includes work needed in propagating fractures and ignores fracture nucleation work because that quantity is usually negligible (Elliott, 1976a).

$$W_{f\text{-quartzite}} = S_e \frac{SA}{V} V_S \text{ J}, \quad (3)$$

where S_e is the surface energy/area of the fracture surfaces, SA/V is the surface area/volume ratio of the outcrop-scale fracture-bound blocks and V_S is the volume of the folded unit.

The work done in forming the outcrop-scale cleavage surfaces within the Pioche argillite is determined by solving for the maximum shear stress (τ_{max}) from the general equation for pressure solution (i.e., Coble creep in the presence of water) and multiplying this value by the total volume of cleavage zones. The general equation for pressure solution is

$$\varepsilon = \frac{\Lambda V D \delta \sigma_{diff}}{RTd^3} e^{\frac{-H}{RT}}, \quad (4)$$

where ε is the strain rate, Λ is a dimensional parameter based on a model for the arrangement of grains, V is the molar volume, D is the diffusion coefficient, δ is the grain boundary width, σ_{diff} is the differential stress, R is Boltzman's constant (8.3 J/(mol K)), T is the absolute temperature, d is the grain size and H is the activation enthalpy for grain boundary diffusion (Knipe, 1989; Farver and Yund, 1991; Twiss and Moores, 1992; Passchier and Trouw, 1996; Blenkinsop, 2000). The maximum shear stress (τ_{max}) is one-half of the σ_{diff} value.

3.3. Shearing along surfaces

The amount of work required to slide along surfaces/zones (to accommodate cataclastic flow) is calculated by first determining how much work is required to slide along one surface (e.g. fracture) and then multiplying this value by the total number of surfaces in the deforming unit. The displacement along each surface/zone is calculated from a power–law relationship between the log of the average zone thickness (t) versus the log of the average displacement along that zone (u), and has the form

$$u = \beta t^{\alpha} \quad (5)$$

where α is the exponent (slope) and β is the pre-exponent (anti-log of the intercept) (Hull, 1988; Mitra, 1993).

The amount of work required to slide on an individual outcrop-scale surface is

$$w_s = \sigma_s u L^2 \text{ J}, \quad (6)$$

where σ_s is the sliding stress, u is the average displacement, and L^2 is the average surface area of each outcrop-scale surface (Elliott, 1976b; Mitra, 1993; Cooke and Murphy, 2004). The sliding stress (σ_s) is estimated by using the Navier–Coulomb fracture criterion,

$$\sigma_s = c + \mu\sigma_n \quad (7)$$

where c is the cohesive strength, σ_n is the normal stress and μ is the coefficient of internal friction.

4. Work results: natural case study

Unraveling the details for the amount of energy consumed during folding of the Pioche unit begins by considering the total work involved. The total amount of work required to emplace a 1 km slice of the CR thrust sheet has already been calculated in a previous paper to be 7×10^{19} J (Ismat and Mitra, 2005a). The principal mechanisms involved in folding (e.g. shearing, kinking, propagation) are the same as those involved in thrust-sheet emplacement. Based on the thrust sheet's work estimate, the volume of the thrust sheet (2.3×10^{12} m^3, for a slice of the thrust sheet 1 km thick) and the volume of the Pioche unit in the fold (4.6×10^8 m^3, for a 1 km thick slice of the thrust sheet), the total amount of work involved in folding the Pioche unit is estimated to be $\sim 1.4 \times 10^{16}$ J.

4.1. Kink folding

The uniaxial compressive strength of argillite is 50–100 MPa and quartzite has a uniaxial compressive strength of >250 MPa (Dewhurst and Jones, 2002; Heesakkers et al., 2007; Mohamed et al., 2008). Since the strength of quartzite is ~3–4× larger than that for argillite, most of the work goes into folding the quartzite and the argillite plays a passive role in the kink folding process. Because of this, work needed for kink folding only the quartzite member is calculated (Fig. 6).

The folding history of the Pioche unit is subdivided into three incremental stages (W_{k1}, W_{k2}, W_{k3}); the relict synformal hinge has been modeled to form in the early stages (W_{k1}) of fold tightening (Fig. 6). The volume of the quartzite unit considered and the kink angle is varied for each stage so that

$$W_k = W_{k1} + W_{k2} + W_{k3}. \quad (8)$$

W_{k1}, W_{k2}, and W_{k3} are all calculated from equation (2). An interbed shear stress (τ_{ib}) of 2×10^7 Pa is used in equation (2), based on long term yield strength (Elliott, 1976b; Ismat and Mitra, 2005a). Substituting these three kink folding values into equation (8),

$$\begin{aligned} W_k &= 3.4 \times 10^{15} \text{ J} + 5.4 \times 10^{15} \text{ J} + 3.0 \times 10^{14} \text{ J} \\ W_k &= 9.1 \times 10^{15} \text{ J}. \end{aligned} \quad (9)$$

4.2. Fracture and cleavage formation

The quartzite member of the Pioche unit is considered for the work involved in forming fractures; the argillite did not fracture, rather it formed early LPS cleavage surfaces. The average SA/V ratio of the outcrop-scale rhomb-shaped fracture-bound blocks is 6.2×10^4 m^{-1}; this value is determined from scaled clay block

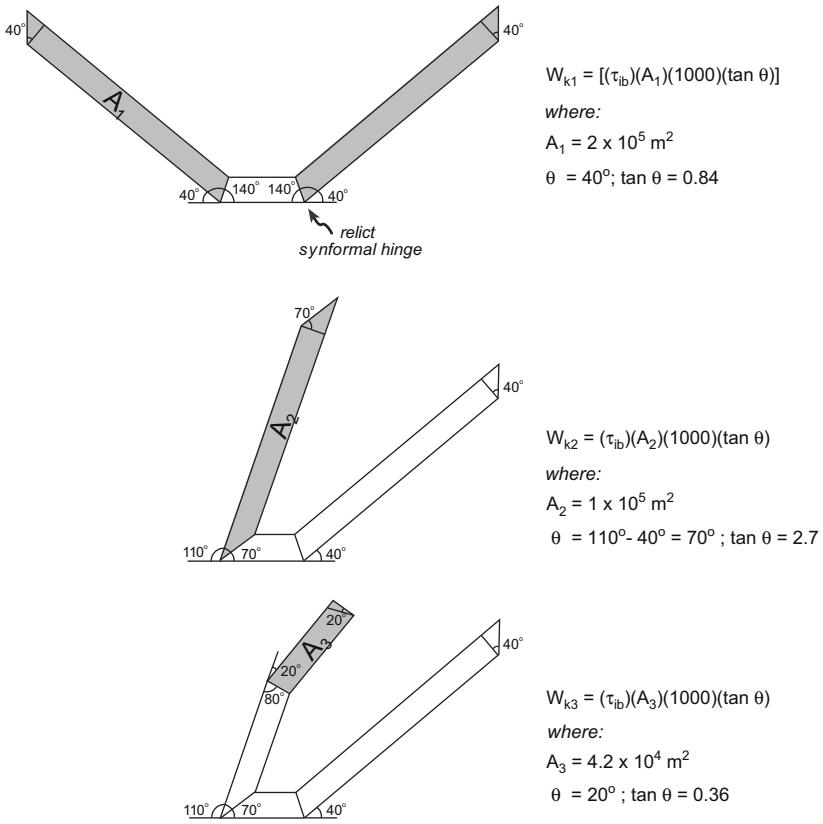

Fig. 6. Kinematic history of the Pioche fold, illustrated as three kink-fold stages (W_{k1}, W_{k2}, and W_{k3}). The volume of both quartzite layers are combined and modeled as one thick layer (see equation (2)). The geometry of the final kink fold (W_{k3}) matches the present-day kink geometry, shown in Fig. 3b.

models (see Ismat and Mitra, 2005a, Data Repository 1, for a detailed description of this method). The folded quartzite volume (V_S) for a unit width of 1000 m is 2.3×10^8 m^3, i.e., half of the volume of the folded Pioche unit. A surface energy/area (S_e) value of 55 J m^{-2} is used (typical values range from 10 to 100 Jm^{-2}); this empirical value includes the energy needed to propagate the plastic zone at the fracture tip (Paterson, 1978; Mitra and Boyer, 1986). Substituting into equation (3)

$$W_{\text{f-quartzite}} = 7.8 \times 10^{14} \text{ J}. \quad (10)$$

The argillite unit comprises the other half of the Pioche unit, i.e., 2.3×10^8 m^3, and is subdivided into rhomb-shaped blocks. The argillite rhombs are delineated by a minimum of two cleavage surfaces. Each cleavage is estimated to be 2 m long (L), 2 m wide, and 0.002 m thick (t), resulting in an average volume of one cleavage surface to be 8×10^{-3} m^3. Approximately 10% of the argillite is comprised of cleavage surfaces, so there are $\sim 2.9 \times 10^9$ total cleavage surfaces within the argillite member, giving a total volume of cleavage surfaces (C_{TOT}) of 2.3×10^7 m^3.

Pressure solution takes place within a range of natural geologic strain rates from 10^{-12} s^{-1} to 10^{-15} s^{-1}. Based on earlier work in the CR (Ismat and Mitra, 2005a) and estimated strain rates for deformation the upper crust (Carter and Tsenn, 1987; Dahlen and Barr, 1989; Jeng et al., 2002), an average strain rate of 10^{-13} s^{-1} is used. Based on experimental work on quartz, an average estimate of 90 is used for Λ (typical values for Λ range from 40 to 140), a V value of 2.6×10^{-5} m^3/mol is used, D is estimated to be 7.5×10^{-7} m^2/s, a δ value of 4×10^{-11} m is input, H is estimated to be 7.4×10^4 J/mol, a d value of 5×10^{-4} is applied, and a T value of 423 K (i.e., 150 °C) is used, based on an average geothermal gradient of ~30 °C/km for this area during folding (Fletcher, 1984; Craddock, 1986; Ismat and Mitra, 2005a). (At 100 MPa mean stress, average temperatures for diffusion range from 100 to 600 °C) (Rutter, 1976; Passchier and Trouw, 1996; Blenkinsop, 2000; Labotka et al., 2000). Substituting these values into equation (4),

$$\sigma_{\text{diff}} = 8.9 \times 10^8 \text{ Pa}. \quad (11)$$

The maximum shear stress (τ_{max}) is one-half of the σ_{diff} value, so that

$$\tau_{\max} = 4.5 \times 10^8 \text{ Pa}. \quad (12)$$

The total amount of work required to form the observed cleavage sets in the Pioche argillite ($W_{\text{f-argillite}}$) is

$$W_{\text{f-argillite}} = \sigma_D C_{TOT} = 1.2 \times 10^{16} \text{ J}. \quad (13)$$

4.3. Shearing along surfaces

The quartzite and argillite members of the Pioche Formation both deformed by (block-supported) cataclastic flow. Fracture networks in the quartzite and cleavage surfaces in the argillite define rhomb-shaped blocks.

The fractures bounding quartzite outcrop-scale blocks are thin, 4–5 sided tabular zones ~0.2 m long (L) and 0.2 m wide with an average thickness (t) of ~0.004 m; the average volume of one fracture surface/zone is $\sim 1.6 \times 10^{-4}$ m^3. In equation (5), β typically ranges from 10 to 1000 (McClintock and Argon, 1966; Reed-Hill, 1973; Hull, 1988; Evans, 1990; Mitra, 1993). Here, a β value of 10 (a conservative estimate using the smallest likely displacement on the surface) is used. An α value of 0.97 is used, which suggests a near linear relationship between zone thickness and displacement along that zone for over seven orders of magnitude. This relationship is based on data from over 113 fault zones that were accommodated

primarily by cataclastic flow (Hull, 1988; Evans, 1990; Mitra, 1993). Substituting into equation (5),

$$u = 4.72 \times 10^{-2} \text{ m}. \quad (14)$$

Based on a detailed analysis of the outcrop-scale fracture morphology, we estimate that ~1% of the quartzite member is made up of outcrop-scale fractures. The volume of the quartzite layer is 2.3×10^8 m^3. Therefore, the total volume of fractures in the quartzite is 2.3×10^6 m^3. From this, we estimate that $\sim 1.4 \times 10^{10}$ outcrop-scale fractures developed within the quartzite member of the Pioche unit.

A cohesive strength (c) of 0.5×10^8 Pa is used for quartzite (Twiss and Moores, 1992; Mandl, 2000; Scholz, 2002). Based on a depth of deformation of ~4–5 km, σ_n is estimated to be 1.1×10^8 Pa. The value for the coefficient of internal friction (μ) used is 0.7; this value is the average of the frictional sliding criterion ($\mu = 0.81$) and the coefficient of internal friction associated with new fracture development for the Coulomb fracture criterion ($\mu = 0.6$) because cataclastic flow occurs by fracturing and sliding (Ismat and Mitra, 2005a). Substituting into equation (7),

$$\sigma_s = 1.3 \times 10^8 \text{ Pa}. \quad (15)$$

From this, and an average displacement (u) of 4.72×10^{-2} m on each fracture surface, the amount of work required to slide along one outcrop-scale fracture is determined from equation (6) to be

$$w_s = 2.5 \times 10^5 \text{ J}. \quad (16)$$

The work required for sliding along all the outcrop-scale fractures is

$$W_{\text{sqtz}-1} = \sum_{w_s} = 3.5 \times 10^{15} \text{ J}. \quad (17)$$

Additional late-stage sliding along fracture networks took place within the west limb, as indicated by slickensided fracture surfaces that are concentrated there. Because of this, an additional component for sliding along the west-limb fracture sets ($W_{\text{sqtz-west limb}}$) is added to the $W_{\text{sqtz}-1}$ value. The volume of the quartzite in the west limb is $\sim 1.17 \times 10^8$ m^3. Therefore, the total volume of the fractures in the west limb is $\sim 1.17 \times 10^6$ m^3, or $\sim 7.3 \times 10^9$ fractures. Using the same value for the amount of work required to slide along one fracture, as calculated in equation (16),

$$W_{\text{sqtz-west limb}} = \sum_{w_s} = 1.8 \times 10^{15} \text{ J}. \quad (18)$$

(Note: it is assumed that the displacements on the surfaces are the same as calculated earlier). So, the total amount of work required to slide on the fractures within the quartzite is

$$W_{\text{s-quartzite}} = W_{\text{sqtz-1}} + W_{\text{sqtz-west limb}} = 5.3 \times 10^{15} \text{ J}. \quad (19)$$

The work involved in sliding along the cleavage surfaces within the Pioche argillite is calculated in a similar manner. But, the following variables considered for the argillite W_s term vary from those used to calculate $W_{\text{s-quartzite}}$. First, the entire volume of the argillite member is considered once; most of the slidings along the cleavage surfaces take place in the later stages of fold tightening and is equally distributed throughout the argillite. Second, an average cleavage thickness of 0.001 m is used resulting in the displacement along each zone (u) to be 1.15×10^{-2} m. (Note that a minimum cleavage thickness is used rather than the measured thickness of 0.002 because the thickness–displacement relationship (equation (5)) is based on surface/zone thicknesses due to shearing). The final variables that are adjusted for the argillite are its coefficient of internal friction (μ) and its cohesive strength. Argillite is much weaker than quartzite; a μ value of 0.4 and a cohesive strength (c) of 0.5×10^7 Pa are used, which results in a sliding stress (σ_s) of 4.9×10^7 Pa.

Substituting into equation (6),

$$w_s = 2.3 \times 10^6 \text{ J} \quad (20)$$

for one cleavage surface. The total work required by all cleavages in the argillite member is

$$W_{\text{s-argillite}} = \sum_{ws} = 6.5 \times 10^{15} \text{ J}. \quad (21)$$

Although the sliding stress for argillite is much smaller than quartzite, the total surface area for all of the cleavages combined is ~21× greater than all of the quartzite surfaces. So, the work involved for sliding along these cleavage surfaces (6.5×10^{15} J) is nearly identical the quartzite W_s term (5.3×10^{15} J).

4.4. Total work

Substituting into equation (1), the total work for the quartzite member of the Pioche unit is

$$W_{\text{t-quartzite}} = 9.1 \times 10^{15} + 7.8 \times 10^{14} + 5.3 \times 10^{15} = 1.5 \times 10^{16} \text{ J}, \quad (22)$$

and the total work for the argillite member is

$$W_{\text{t-argillite}} = 0 + 1.2 \times 10^{16} + 6.5 \times 10^{15} = 1.8 \times 10^{16} \text{ J}. \quad (23)$$

So, the total calculated work required for folding the Pioche unit is

$$W_t = W_{\text{t-quartzite}} + W_{\text{t-argillite}} = 3.3 \times 10^{16} \text{ J}. \quad (24)$$

This calculated total work value is very close (i.e., same order of magnitude) to the predicted estimate of 1.4×10^{16} J, which is based on the Pioche unit's fraction of the total CR thrust-sheet work estimate. Additionally, the $W_{\text{tquartzite}}$ and the $W_{\text{targillite}}$ are similar in value. Many models suggest that the incompetent member plays a passive role in the folding process. The work values (equations (22)–(24)), however, indicate that the incompetent member, which comprises half of the Pioche unit, uses approximately half (54%) of the total energy. The question remains as to how each layer behaved and assisted various kinematic components of folding.

5. Data analysis using Bayly's model

Various combinations of mechanisms (e.g. kink folding, fracture formation, and sliding along surfaces) accommodate different kinematic components of folding at each increment of fold tightening. The same five basic kinematic components of folding first modeled by Bayly (1974) (limb shear, limb thickening/thinning, hinge shear, hinge thickening/thinning, and hinge curvature) are tracked using the folded Pioche unit of the CR syncline. Variables unique to the CR syncline at each stage of folding (e.g. bed thickness) are input into equations of Bayly (1974) to calculate how much energy is consumed by each of the five kinematic components during fold tightening (Fig. 7a and b).

The behavior of each of the five kinematic components for the Pioche unit during different increments of fold tightening is plotted on three sets of graphs (Fig. 7a and b). The equations used assume that the fold is upright and symmetrical. Because of this, successive folding stages are represented with increasing limb dips. The

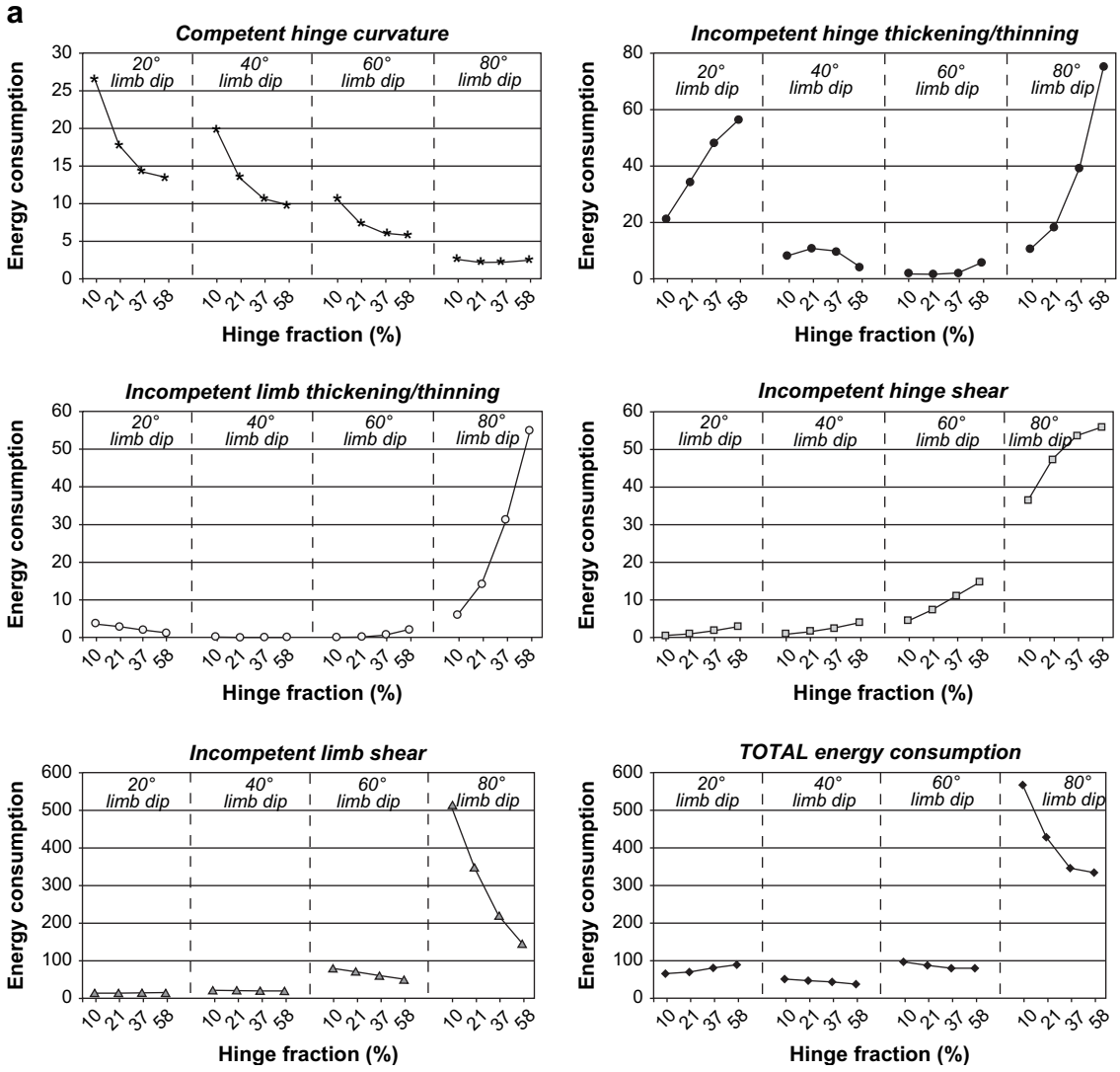

Fig. 7. Graphs showing energy consumption by each of the five kinematic components of folding (see Fig. 1). Symmetrical, upright folds are assumed, so fold geometry is classified by limb dips. h_1, h_2 and j_2 are adjusted for each fold geometry as follows. Assuming that the undeformed thickness of the argillite layer is 115 m and the undeformed thickness of one of the quartzite layers is 57 m, then at 20° limb dip: $h_1 = 57$ m, $h_2 = 115$ m, $j_2 = 115$ m; 40° limb dips: $h_1 = 57$ m, $h_2 = 131$ m, $j_2 = 107$ m; 60° limb dips: $h_1 = 57$ m, $h_2 = 148$ m, $j_2 = 49$ m; 80° limb dips: $h_1 = 57$ m, $h_2 = 164$ m, $j_2 = 33$ m. For other variable values input (e.g. competency contrasts), refer to appendix. (a) Set I is plotted in terms of non-dimensional values, which are normalized by the viscosity of the incompetent layer. The absolute work values can be calculated by multiplying the non-dimensional values by the viscosity of the incompetent layer. (b) Set II is plotted in terms of percent energy consumption versus hinge fraction for four different fold geometries. (c) Energy consumption for the present-day geometry of the CR syncline using equations of Bayly (1974) and a summation of the mechanisms involved in each kinematic component.

graphs illustrate the patterns of energy consumption for four different hinge fractions (10%, 21%, 37%, 58%) for limb dips of 20°, 40°, 60° and 80° (i.e., interlimb angles of 140°, 100°, 60°, and 20°, respectively) (Fig. 7a). The hinge fraction percentages and limb dips chosen cover a wide range of natural fold shapes.

The first set of graphs (Set I) display the general patterns of each kinematic component of folding separately as well as the combined energy consumption for each limb dip (Fig. 7a). The second set (Set II) is grouped by limb dip and the data are plotted in terms of percentage in order to more clearly display the relative contributions of each of the kinematic components at each stage of fold tightening (Fig. 7b). In the third set of graphs, the fold geometry that most closely matches the final state of the CR syncline is examined more closely. The core of the CR syncline has an interlimb angle of ~52° and a western-limb dip of 82°. In addition, ~1/3 of the folded Pioche unit makes up the hinge region of the present-day geometry. So, the results for a fold with an 80° limb dip and a 37% hinge fraction are used (Fig. 7b and c). These results are compared against the amount of work required to form the CR syncline, which is calculated by summing the mechanisms used in the Pioche quartzite and argillite layers (Fig. 7c, Table 2). Details from all three sets of graphs are described below.

5.1. Set I graph results

The first set of graphs suggest that the total amount of energy required for folding is lower at 40° limb dips than at any other stage of fold tightening (Fig. 7a). In many multilayer folding models, 40° is considered to be the 'critical threshold' for the competent unit, and so the rate of folding increases once this threshold is passed. Soon after this threshold is reached, the incompetent member strongly influences the folding process (Ramsay, 1974; Williams, 1980).

In the CR syncline, beyond limb dips of ~40° (i.e., an interlimb angle of ~100°), only one of the fold hinges within the Pioche unit remained active (Figs. 3b, 5a and 6). At this stage, Pioche argillite was transported from the fold limbs to the final hinge

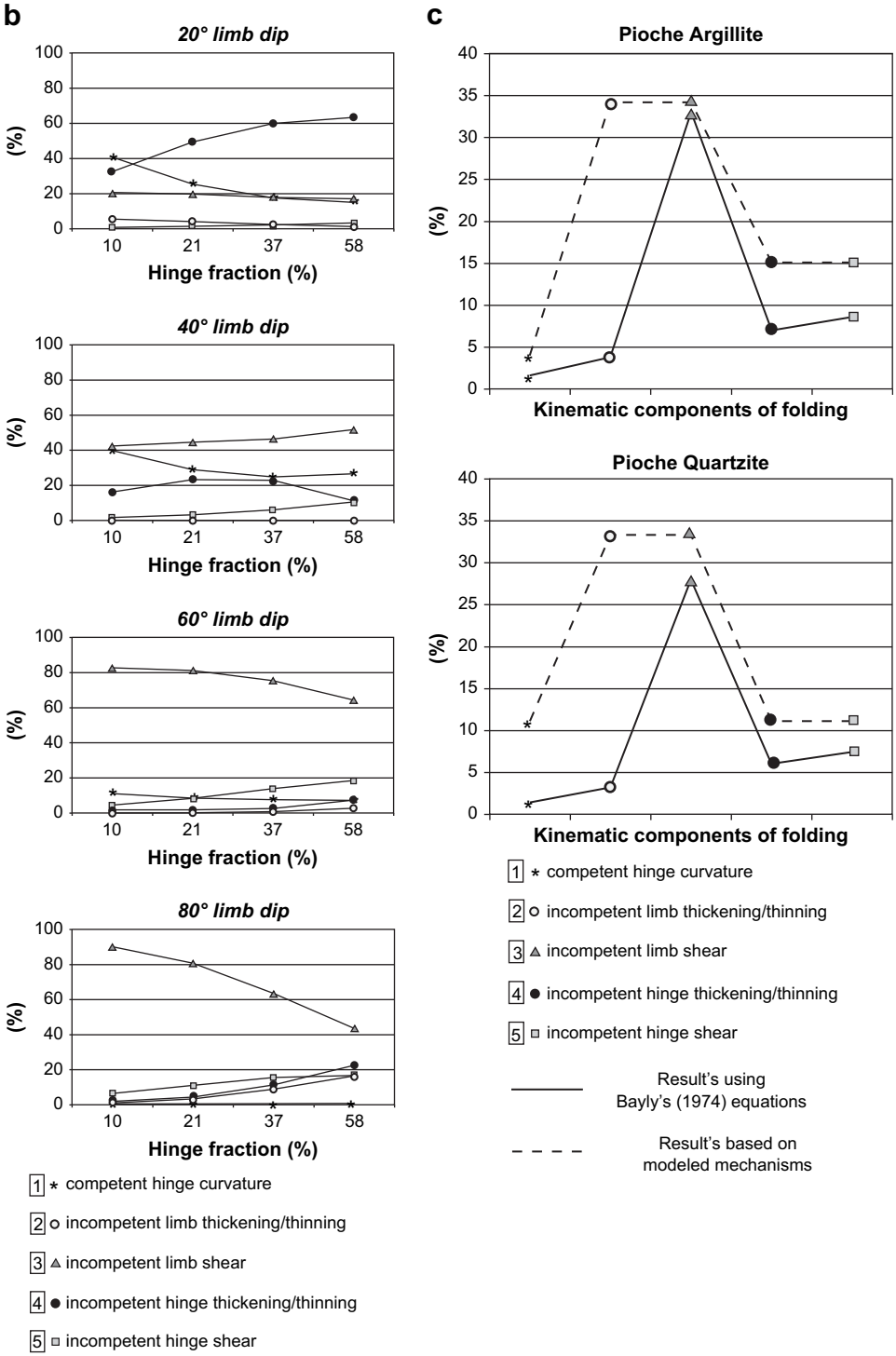

Fig. 7. (*continued*).

location. The incompetent layer's influence in driving the Pioche fold shape is marked by this argillite transport (Fig. 5a and b). So, the kinematics of the CR syncline agrees with the predicted behavior of incompetent unit(s) for multilayer folds (Donath and Parker, 1964; Williams, 1980).

Fig. 7a also reveals that with tighter folds, less total energy is consumed with increasing hinge fractions. In the CR syncline, however, the activity of only one of the two hinges beyond 40° limb dips suggests that the hinge fraction decreased as the fold tightened. So, in order to minimize energy consumption, the hinge zone fraction for the CR syncline may have increased with material transport from the limbs to the active hinge. This potential reduction in energy consumption may provide an alternative explanation for the large amount of material that was transported from the limbs to the hinge as the fold tightened.

Although the total energy consumption is a minimum at 40° limb dips, many of the individual kinematic components do not show a minimum at 40° limb dips. Details of the relative contributions of each of the kinematic components are described in the following section using Fig. 7b.

Table 2
Breakdown of percent energy consumption, for the present-day geometry of the CR syncline, based on a summation of the mechanisms involved in each kinematic component.

	Kinemetic Components	Using Bayly (1974) equations		Summation of mechanisms used		
		%	Joules	Mechanisms	%	Joules
Cambrian Pioche quartzite	Competent hinge curvature	1.4	4.6×10^{14}	$W_sW_fW_k$	11.1	1.7×10^{15}
	Incompetent limb thickening/thinning	3.2	1.0×10^{15}	$W_sW_fW_k$	33.3	5.0×10^{15}
	Incompetent limb shear	28	9.2×10^{15}	$W_sW_fW_k$	33.3	5.0×10^{15}
Competent	Incompetent hinge thickening/thinning	6	2.0×10^{15}	$W_sW_fW_k$	11.1	1.7×10^{15}
	Incompetent hinge shear	7.4	2.4×10^{15}	$W_sW_fW_k$	11.1	1.7×10^{15}
	Total	46	1.5×10^{16}	–	100	1.5×10^{16}
Cambrian Pioche argillite	Competent hinge curvature	1.6	5.3×10^{14}	W_s	4	7.2×10^{14}
	Incompetent limb thickening/thinning	3.8	1.3×10^{15}	W_sW_f	34.2	6.2×10^{15}
	Incompetent limb shear	33	1.1×10^{16}	W_sW_f	34.2	6.2×10^{15}
Incompetent	Incompetent hinge thickening/thinning	7	2.3×10^{15}	W_sW_f	15.1	2.7×10^{15}
	Incompetent hinge shear	8.6	2.8×10^{15}	W_sW_f	15.1	2.7×10^{15}
	Total	54	1.8×10^{16}	–	100	1.8×10^{16}

5.2. Set II graph results

Based on the results from the graphs in Fig. 7b and the kinematic details of the CR syncline, we can re-evaluate the roles of competent and incompetent units. Using the term 'competency' as defined earlier, competent layers maintain constant orthogonal thickness and undergo minimal internal deformation, i.e., maintain a class-1B fold shape. Incompetent members, however, maintain contact between competent layers by thickening in the hinge region and thinning in the limbs, thereby attaining a shape close to a class-3 fold. The question is if the roles of the competent and incompetent layers can be reversed and/or become indistinguishable at some stage during folding. To answer this, the behavior of the Pioche quartzite and argillite are compared and examined for a wide range of fold geometries (Fig. 7b).

With 20° limb dips, the hinge thickening/thinning of the incompetent member and the hinge curvature of the competent member components consume ~70% of the total energy, most of which is accomplished by thickening/thinning of the incompetent member (Fig. 7b). But, previous work on other units within the CR syncline (Ismat and Mitra, 2005b) shows that there is minimal transport of incompetent units (e.g. Proterozoic Inkom shale) (Fig. 3a) until the fold reached limb dips of 40°. During the early stages of folding, the CR syncline adjusted bed thicknesses by intense cataclastic flow within the hinge region of the competent quartzite units (e.g. Proterozoic Caddy Canyon, Eocambrian Tintic) (Fig. 3a) (Ismat and Mitra, 2001a, 2005a,b). This behavior is extended to the Pioche unit, which implies that the hinge thickness changes took place in the early stages of folding primarily by cataclastic flow within the Pioche quartzite member. The uniaxial compressive strength of quartzite cataclasite (~97 MPa) is comparable to the uniaxial compressive strength of argillite (50–100), which is ~1/3 the strength of quartzite (>250) (Dewhurst and Jones, 2002; Heesakkers et al., 2007; Mohamed et al., 2008). So, at 20° limb dips, the cataclasite quartzite member within the hinge region behaved as the *incompetent* layer.

Once the fold reaches limb dips of 60°, limb shear of the incompetent member (Pioche argillite) dominates the energy consumption (Fig. 7b). Beyond 40° limb dips, argillite was transported from the limbs to the hinge, causing quartzite layers to move closer together in the limb region and drift apart in the hinge region (via cataclastic flow) to accommodate these thickness changes. The incompetent limb shear component documents this argillite transport from the limbs and accounts for ~75% of the total energy consumed, while all the incompetent components combined use ~90% of the total energy (Fig. 7b). The work equations (equations (22)–(24)), however, suggest that the incompetent member should account for approximately half of the total work required (Table 2). So, at this stage of folding, the originally competent quartzite layer may have in fact behaved as an *incompetent* layer as it deformed by cataclastic flow. In other words, deformation in the competent quartzite, although not plotted separately, is actually incorporated into the incompetent limb deformation values (Table 2, Fig. 7b).

In addition to the 'competency' of originally *competent* and *incompetent* units evolving during fold tightening, the role of the limbs and hinge may change. At 20° limb dips, hinge curvature and hinge thickening/thinning consume the largest fraction of total energy (~70% combined) (Fig. 7b). At 80° limb dips, limb thickening/thinning and limb shear are the major consumers of energy (~62% combined, for 58% hinge fraction) (Fig. 7b). In other words, the hinge and limb kinematic components essentially switch roles as the major consumer of energy during fold tightening. What this suggests about which kinematic components have a larger influence on fold shape during different increments of fold tightening are still unclear.

5.3. Set III graph results

Selected variables (see Appendix) representing the Pioche quartzite and argillite were input into equations of Bayly (1974) to estimate how much energy each of the five kinematic components of folding consumed at various stages of fold tightening. Results from these equations for a fold with an 80° limb dip and a hinge fraction of 37% suggest that, 3% of the total energy consumed is used to accommodate competent hinge curvature, 7% is used for incompetent limb thickening/thinning, 61% is used for incompetent limb shear, 13% is used for incompetent hinge thickening/thinning, and 16% is used for incompetent hinge shear (Fig. 7b and c). The quartzite and argillite consume 46% and 54% of the total consumed energy, respectively. The total percentage values estimated for each component are divided as such for the Pioche quartzite and argillite (Table 2).

This percentage breakdown is compared to work values calculated for the mechanisms (kink folding, fracture formation, and sliding along surfaces) used in each kinematic component of folding (Fig. 7c, Table 2). Various combinations of the three different mechanisms discussed here are used in each of the five kinematic components. Different mechanisms are assigned for each kinematic component in both the quartzite and argillite layers making up the core of the CR syncline.

The following method is used to calculate energy consumption, based on folding mechanisms, in each layer. First, the work values assigned for each mechanism are subdivided into three equal parts, two limbs and one hinge region, because the hinge region makes up ~1/3 of the folded Pioche unit. Then the hinge and limb regions are analyzed separately for the different mechanisms that are assumed to be involved in the hinge and limbs. The values for all mechanisms used in each component are totaled and compared to the results based on applying equations of Bayly (1974) (Fig. 7c).

5.3.1. Mechanisms used in the Pioche quartzite

9.1×10^{15} J is required to kink the Pioche quartzite (W_k) and 1/3 of this value is consumed by the hinge region where

$$W_{\text{k-qtzite-hinge}} = W_k\frac{1}{3} = \left(9.1 \times 10^{15}\right)\frac{1}{3} = 3 \times 10^{15}\ \text{J}. \quad (25)$$

Three components (hinge curvature, hinge thickening/thinning and hinge shear) are modeled here as being equally assisted by kinking where

$$W_{\text{k-qtzite-hinge-curvature}} = W_{\text{k-qtzite-hinge-thick}} = W_{\text{k-qtzite-hinge-shear}} = 1 \times 10^{15}\ \text{J} \quad (26)$$

Deformation in the hinge region is also assisted by the formation of fractures (W_f) and sliding (W_s) along those fractures. 1/3 of the fractures are in the hinge region where

$$W_{\text{f-qtzite-hinge}} = \left(W_{\text{f-qtzite}}\right)\frac{1}{3} = \left(7.8 \times 10^{14}\right)\frac{1}{3} = 2.6 \times 10^{14}\,\text{J} \quad (27)$$

and

$$W_{\text{s-qtzite-hinge}} = (W_{\text{s-qtzite}})\frac{1}{3} = \left(5.3 \times 10^{15}\right)\frac{1}{3} = 1.76 \times 10^{15}\ \text{J}. \quad (28)$$

It is assumed here that fracturing and sliding support the same three kinematic components in the hinge region equally so that

$$W_{\text{f-qtzite-hinge-curvature}} = W_{\text{f-qtzite-hinge-thick}} = W_{\text{f-qtzite-hinge-shear}} = 8.7 \times 10^{13}\,\text{J}. \quad (29)$$

and

$$W_{\text{s-qtzite-hinge-curvature}} = W_{\text{s-qtzite-hinge-thick}} = W_{\text{s-qtzite-hinge-shear}} = 5.8 \times 10^{14}\,\text{J} \quad (30)$$

The total amount of work required by the quartzite layer is 1.5×10^{16} J. So, the percentage of work required to assist deformation in the hinge region of the Pioche quartzite by hinge curvature, hinge thickening/thinning and hinge shear is

$$W_{\text{qtzite-hinge-curvature}} = \left(\frac{1 \times 10^{15} + 8.7 \times 10^{13} + 5.8 \times 10^{14}}{1.5 \times 10^{16}}\right)100 = 11.1\%, \quad (31)$$

and

$$W_{\text{qtzite-hinge-thick}} = \left(\frac{1 \times 10^{15} + 8.7 \times 10^{13} + 5.8 \times 10^{14}}{1.5 \times 10^{16}}\right)100 = 11.1\%, \quad (32)$$

and

$$W_{\text{qtzite-hinge-shear}} = \left(\frac{1 \times 10^{15} + 8.7 \times 10^{13} + 5.8 \times 10^{14}}{1.5 \times 10^{16}}\right)100 = 11.1\%. \quad (33)$$

The quartzite in the limbs of the fold accommodates folding by using the same three mechanisms as used in the hinge region. Both of the limbs make up 2/3 of the total volume so that

$$W_{\text{k-qtzite-limbs}} = W_k\frac{2}{3} = \left(9.1 \times 10^{15}\right)\frac{2}{3} = 6 \times 10^{15}\ \text{J}. \quad (34)$$

Limb thickening/thinning and limb shear are modeled here to be assisted equally by kinking so that

$$W_{\text{k-qtzite-limbs-thick}} = W_{\text{k-qtzite-limbs-shear}} = 3 \times 10^{15}\ \text{J}. \quad (35)$$

Using the same method of analysis as described above, fracture formation (W_f) and sliding (W_s) along those fractures in the limbs requires

$$W_{\text{f-qtzite-limbs}} = \left(W_{\text{f-qtzite}}\right)\frac{2}{3} = \left(7.8 \times 10^{14}\right)\frac{2}{3} = 5.2 \times 10^{14}\ \text{J} \quad (36)$$

and

$$W_{\text{f-qtzite-limbs}} = (W_{\text{s-qtzite}})\frac{2}{3} = \left(5.3 \times 10^{15}\right)\frac{2}{3} = 3.52 \times 10^{15}\ \text{J}. \quad (37)$$

Limb thickening/thinning and limb shear are modeled here as being equally assisted by W_f and W_s, so that

$$W_{\text{f-qtzite-limbs-thick}} = W_{\text{f-qtzite-limbs-shear}} = 2.6 \times 10^{14}\ \text{J} \quad (38)$$

and

$$W_{\text{s-qtzite-limbs-thick}} = W_{\text{s-qtzite-limbs-shear}} = 1.76 \times 10^{15}\ \text{J}. \quad (39)$$

The percentage of work required to assist deformation in the limbs of the quartzite layer is

$$W_{\text{qtzite-limbs-thick}} = \left(\frac{3 \times 10^{15} + 2.6 \times 10^{14} + 1.76 \times 10^{15}}{1.5 \times 10^{16}}\right)100 = 33.3\%, \quad (40)$$

and

$$W_{\text{qtzite-limbs-shear}} = \left(\frac{3 \times 10^{15} + 2.6 \times 10^{14} + 1.76 \times 10^{15}}{1.5 \times 10^{16}}\right)100 = 33.3\%. \quad (41)$$

5.3.2. Mechanisms used in the Pioche argillite.

The total amount of work required to form the cleavage sets in the argillite ($W_{\text{f-argillite}}$) is 1.2×10^{16} J. The hinge region consumes 1/3 of this amount, so that

$$W_{\text{f-argillite-hinge}} = 4 \times 10^{15}\ \text{J}. \quad (42)$$

Hinge thickening/thinning and hinge shear likely are assisted by W_f in the hinge region. $W_{\text{f-argillite-hinge}}$ is divided equally between these two kinematic components where

$$W_{\text{f-argillite-hinge-thick}} = W_{\text{f-argillite-hinge-shear}} = 2 \times 10^{15}\ \text{J}. \quad (43)$$

Deformation in the hinge region is also assisted by sliding along cleavage surfaces where

$$W_{\text{s-argillite}} = 6.5 \times 10^{15}\ \text{J}. \quad (44)$$

The hinge region uses 1/3 of this value, so that

$$W_{\text{s-argillite-hinge}} = 2.16 \times 10^{15}\ \text{J}, \quad (45)$$

and assists three components (hinge curvature, hinge thickening/thinning and hinge shear). The amount of work required to slide along cleavage surfaces is modeled here to be divided equally between these three components where

$$W_{\text{s-argillite-hinge-curvature}} = W_{\text{s-argillite-hinge-thick}} = W_{\text{s-argillite-hinge-shear}} = 7.2 \times 10^{14}. \quad (46)$$

The total amount of work required by the argillite layer is 1.8×10^{16} J. The percentage of work required to deform the hinge region by hinge curvature is

$$W_{\text{argillite-hinge-curvature}} = \left(\frac{7.2 \times 10^{14}}{1.8 \times 10^{16}}\right)100 = 4\%. \quad (47)$$

The percentage of work required by hinge thickening/thinning is

$$W_{\text{argillite-hinge-thick}} = \left(\frac{2\times10^{15}+7.2\times10^{14}}{1.8\times10^{16}}\right)100 = 15.1\%, \quad (48)$$

and the percentage of work required by hinge shear in the argillite is

$$W_{\text{argillite-hinge-shear}} = \left(\frac{2\times10^{15}+7.2\times10^{14}}{1.8\times10^{16}}\right)100 = 15.1\%. \quad (49)$$

The argillite in the limbs of the fold accommodated deformation using the same two mechanisms. Both of the limbs make up 2/3 of the total volume of the argillite. Therefore, the amount of work required to form cleavage surfaces ($W_{\text{f-argillite}}$) in the limbs is

$$W_{\text{f-argillite-limb}} = \left(W_{\text{f-argillite}}\right)\frac{2}{3} = \left(1.2\times10^{16}\right)\frac{2}{3} = 8\times10^{15}\,\text{J}. \quad (50)$$

Limb thickening/thinning and limb shear are modeled here to be assisted equally by cleavage formation, so that

$$W_{\text{f-argillite-limb-thick}} = W_{\text{f-argillite-limb-shear}} = 4 \times 10^{15}\ \text{J}. \quad (51)$$

6.5×10^{15} J is required for shearing along cleavage surfaces ($W_{\text{s-argillite}}$). 2/3 of this is consumed in the limbs, so that

$$W_{\text{s-argillite-limbs}} = \left(6.5 \times 10^{15}\right)\frac{2}{3} = 4.32 \times 10^{15}\ \text{J}. \quad (52)$$

Limb thickening/thinning and limb shear are modeled here to be equally assisted by shearing along cleavage surfaces, so that

$$W_{\text{s-argillite-limb-thick}} = W_{\text{s-argillite-limb-shear}} = 2.16 \times 10^{15}\ \text{J}. \quad (53)$$

The percent of work required to deform the limbs by changing the thickness of the argillite layer and shearing within the argillite layer are modeled here to be equivalent, so that

$$\begin{aligned} W_{\text{argillite-limb-thick}} &= W_{\text{argillite-limb-shear}} \\ &= \left(\frac{4 \times 10^{15} + 2.16 \times 10^{15}}{1.8 \times 10^{16}}\right)100 \\ &= 34.2\%. \end{aligned} \quad (54)$$

5.3.3. Work distribution using equations of Bayly (1974) and folding mechanisms.

The percent distribution for the amount of work required to deform the Pioche quartzite and argillite is calculated here by using (1) equations of Bayly (1974) and (2) by summing the total value of the mechanisms involved in each kinematic component. Results from both methods are comparable for all of the kinematic components, except for limb shear (Fig. 7c). For both the argillite and quartzite layers, the limb shear values calculated based on the total of the mechanisms used to assist limb shear is ~9–10 times greater than the values calculated using equations of Bayly (1974).

Limb shear is modeled here as being primarily assisted by W_s, i.e., the work required to slide along surfaces, such as cleavage surfaces and fractures. Sliding on a distributed network of surfaces, i.e., (block-supported) cataclastic flow, was used to deform the Pioche unit. The W_s value makes up ~36% of the total work involved in deforming the argillite and ~35% of the total work involved in deforming the quartzite.

The amount of work required to accommodate limb shear may not be comparable between these two methods used for calculating energy consumption for the following reasons. (1) The work required to deform the layers by cataclastic flow may involve more work than is often considered, and so may be overlooked by some models, such as Bayly (1974). (2) Alternatively, the work required to deform a material by cataclastic flow may be over-estimated, and so the results based on equations of Bayly (1974) may be more accurate. But, the work estimates for thrust-sheet emplacement via cataclastic flow are comparable to the work required to emplace thrust sheets that are deforming by crystal–plastic mechanisms (Ismat and Mitra, 2005a). Therefore, reason (2) may be unlikely. (3) A more plausible explanation may be that the equal distribution of the mechanisms used to assist the kinematic components of folding resulted in erroneous values. Unfortunately, the field data do not provide sufficient controls on how to distribute various proportions of each mechanism amongst the five kinematic components.

6. Discussion

6.1. Comparison with some multilayer models

Natural folds can have very complex geometries and the kinematic histories for the development of folds and fold-related structures are not always clear; crosscutting relationships are often ambiguous and/or not well preserved. Because of this, we tend to turn to physical, theoretical, and/or computer models to help understand the development of natural folds and other structures associated with folding. Current models that are most applicable to natural folds address folding of *multilayers*, which are composed of an alternating sequence of *competent* and *incompetent* units (e.g. Ramberg, 1964; Johnson and Ellen, 1974; Summers, 1979; Williams, 1980; Mancktelow and Abbassi, 1992; Hunt et al., 1996; Zhang et al., 1996; Cooke et al., 2000; Jeng et al., 2002; Patton and Watkinson, 2005).

Most multilayer folding models show that during fold tightening, the competent layer(s) initially controls the fold shape. However, beyond limb dips of ~20° (i.e., ≤140° interlimb angle), the incompetent layers begin to strongly influence fold geometry (Ramsay, 1974; Williams, 1980; Mancktelow and Abbassi, 1992). Analysis of Bayly (1974) concurs with many other folding models in that the competent unit controls the folding process up to limb dips of ~40° (i.e., an interlimb angle of ~100°) (Ramsay, 1974; Williams, 1980; Hunt et al., 1996; Jeng et al., 2002). In other words, the competent member consumes more energy than the incompetent member during the early stages of fold tightening. By the time the fold reaches limb dips of ~60° (i.e., an interlimb angle of ~60°), the incompetent member consumes most of the energy used in folding.

A similar pattern of behavior is also suggested by the CR syncline. But, during the later stages of folding (≤60° interlimb angles), *both* the competent quartzite and the incompetent argillite influence the fold's geometry as the layers change shape via cataclastic flow (Ismat and Benford, 2007). In other words, the competent layer begins to 'soften' and flow with the incompetent layer(s) (Ord, 1991; Guiton et al., 2003). Several analog models allude to a similar behavior (Zhang et al., 1996; Guiton et al., 2003).

One way in which the competent layer may control a fold's shape in its early stages of development is by producing irregular fold geometries, such as multiple hinges (Zhang et al., 1996). Recent folding models have shown that at some point, only one of several hinges will continue to amplify, so that the fold begins to localize (Hunt et al., 1996; Zhang et al., 1996). One potential explanation suggests that the degree of strain softening throughout the competent layer(s) may influence which hinge amplifies. These models also reveal that during the later stages, once the incompetent unit starts to play a larger role in influencing the fold shape, the multiple hinges

are still preserved, although subdued (Zhang et al., 1996). This argument may explain the origin of the double-kink box-fold geometry within the Pioche Formation of the CR syncline.

6.2. Bending versus stretching

The graphs in Fig. 7a suggest that tighter folds consume less energy with larger hinge fractions. This pattern may indicate how the fold balances the proportion of *bending* and *stretching* of the hinge (comparable to *kinking* and *outer are extension*, respectively). The terminology is derived from current research on folding of single thin sheets which suggests that folds tend toward shapes whose hinges accommodate 20% stretching and 80% bending; this fold shape consumes the least amount of energy (Kunzig, 2003; DiDonna, 2004). A single, large rounded hinge minimizes the curvature, and thus the bending energy, but requires significant stretching. So, more stretching is required for one large rounded hinge and more bending is required for multiple, small angular hinges (Lobkovsky et al., 1995; Matan et al., 2002; Kunzig, 2003; DiDonna, 2004). If a fold hinge remains rounded during tightening, the fold shape will have a larger proportion of stretching than is ideal to satisfy minimum energy requirements. In other words, the dimensions of the hinge zone play a significant role in influencing fold geometry.

As the CR syncline tightened, the Pioche unit may have balanced the competing factors of 'bending' and 'stretching' in two ways. (1) In the early stages of folding, the Pioche unit likely had a double-kink box fold shape. The box fold had minimum interlimb angles of ~140°. This open geometry would require nominal stretching, possibly accounting for less than 20% of the total energy. However, angular hinges require a significant amount of bending energy; *two* angular hinges would require even more, possibly beyond 80% of the total energy. So, continuing folding with only one hinge may have offset this imbalance of stretching and bending. (2) The present-day hinge of the Pioche fold is rounded. As the interlimb angle decreased during fold tightening, the stretching in the hinge region would have increased – possibly beyond the ideal 20%. One way to compensate for this excessive stretching may have been with the formation of late-stage parasitic folds within the hinge region. The parasitic folds are smaller and have multiple hinges, and so require more bending energy than the first-order fold. This suggests that the amount of bending and stretching energy consumed may be balanced across scales. So, the parasitic folds may have a role beyond simply accommodating space problems within the hinge region.

7. Conclusions

This analysis of the multilayer Pioche Formation of the CR syncline has shown the following.

1. In this tight multilayer fold, the *competent* quartzite and *incompetent* argillite members consumed equal amounts of energy during folding.
2. Much of the folding was assisted by cataclastic flow in both the quartzite and argillite layers.
3. The roles of original competent and incompetent layers may reverse during folding. Moreover, both may behave as competent or incompetent layers at various folding stages.
4. As the fold tightened, less energy was consumed with *larger* hinge fractions.
5. The least amount of energy was consumed with 40° limb dips (i.e., 100° interlimb angle).
6. With an interlimb angles ≥140°, the hinge region consumed ~70% of the fold's total energy. As the fold tightened, the limbs begin to consume more of the fold's energy. Once the fold reached an interlimb angle of ~60°, the limbs consume close to 70% of the total energy; the limb shear component accounts for ~3/4 of this 70%.
7. When the syncline tightened beyond an interlimb angle of ~60°, the *incompetent* layer(s) consumed ~90% of the fold's energy.

Acknowledgments

A Franklin & Marshall COG grant helped to support this research. I would like to thank T. Engelder (special editor), D. Wiltschko (associate editor), M. Cooke (reviewer) and an anonymous reviewer for their detailed, thoughtful and encouraging comments. I also thank Stefan Schmalholz and Jean-Pierre Borg for their comments on an earlier version of this paper. Discussions with G. Mitra were very helpful while writing this paper. Finally, I would like to thank B. Benford and P. Riley for their assistance in the field.

Appendix

The following equations, originally derived by Bayly (1974), are used to calculate the relative values of energy consumed for each of the five kinematic components of folding, assuming plane strain and constant area. The same variables used by Bayly (1974) are applied here, for the purpose of direct comparison (Fig. 1b).

Competent member hinge curvature

Energy consumed in hinge curvature of the competent layer is defined by

$$\frac{8N(d\alpha)^2 h_1^3}{3l} \tag{A1}$$

where l is the median length of the hinge zone and h_1 is one-half of the thickness of the competent unit (Fig. 1b). N is the ratio of the competency contrast of the competent and incompetent layers for layer-parallel linear strain; typical values range from 2 to 100 (Dieterich, 1970; Bayly, 1974). Based on the cohesive strengths of the Pioche quartzite and argillite and previous work on multilayer folds composed of similar rock types (Dieterich, 1970; Bayly, 1974; Dewhurst and Jones, 2002; Heesakkers et al., 2007; Mohamed et al., 2008), an average value of $N = 10$ is used (Mancktelow and Abbassi, 1992). α is the limb dip, so dα is the change in dip and

$$d\alpha = \frac{(l\alpha \sin\ \alpha) + (k\alpha^2 \cos\ \alpha E)}{(k\alpha^2 \sin\ \alpha) + (l \sin\ \alpha) - (l\alpha \cos\ \alpha)}, \tag{A2}$$

where E is strain axial ratio in the competent member and is calculated to be 1.6 (Fig. 1a) (Ismat and Mitra, 2001a). This strain axial ratio value is based on bed thickness changes in the competent Proterozoic quartzite layers of the CR syncline, resulting from deformation by (block-supported) cataclastic flow (Ismat and Mitra, 2001a).

Incompetent limb thickening/thinning

Energy consumed in the change in thickness and length of the incompetent member is defined by

$$4mVe^2 \tag{A3}$$

where m is the viscosity of the incompetent member for layer-parallel linear strains; a typical value of $m = 1$ is used (Dieterich, 1970; Bayly, 1974). V measures the average length and thickness of the incompetent limb and is determined from the formula

$$V = 2kj_2 \tag{A4}$$

where k is the median length of the limb and j_2 is half of the incompetent limb's thickness, measured from the mid-point of k

(Fig. 1b). The e value in equation (A3) measures the homogeneous strain in the incompetent limb and is defined by

$$e = \frac{dj_2}{j_2} \tag{A5}$$

where

$$dj_2 = (\cos\ \alpha dh_2) - (H\sin\ \alpha d\alpha). \tag{A6}$$

The incompetent and competent members are interdependent, since plane strain and constant area are assumed. Because of this, the change in thickness of the competent unit (dh_2) is incorporated into the component of incompetent limb thickening/thinning and is equivalent to EH. H measures one-half of the competent/incompetent sequence, i.e., is equal to $h_1 + h_2$ (Fig. 1b). More specifically,

$$H = \frac{h_1\alpha(U+1)(l+k)}{(l\sin\ \alpha) + (\alpha k\cos\ \alpha)} \tag{A7}$$

where U is the area ratio of the incompetent to the competent material, and here is equal to 1 (Fig. 4).

Incompetent limb shear

The energy consumed for layer-parallel shear is determined from the equation

$$nVg^2 \tag{A8}$$

where n is the ratio of the competency of layer-parallel shear strain in the incompetent limb to the competency of layer-parallel linear strain in the incompetent limb. For incompetent layers that are significantly foliated, such as the Pioche argillite, a value of $n = 1/10$ is used. g is the value for layer-parallel shear strain on the limb and is estimated to be

$$g = (\sin\ \alpha dH) + \frac{H\cos\ \alpha d\alpha}{2} \tag{A9}$$

where

$$dH = dh_2 = EH. \tag{A10}$$

Incompetent hinge thickening/thinning

The energy consumed for thickening/thinning in the hinge region is defined by

$$\left(\frac{2ml}{3}\right)\left[\left(\frac{dh_2}{h_2}\right)^2(3h_2 + j_2)\right] + \left[\left(\frac{dh_2}{h_2}\right)\left(\frac{dj_2}{j_2}\right)(2h_2 + 2j_2) + \left(\frac{dj_2}{j_2}\right)^2(j_2 + 3h_2)\right] \tag{A11}$$

Incompetent hinge shear

The energy consumed for layer-parallel shear in the hinge region is determined from the formula

$$\frac{(ng^2l)(h_2 + 3j_2)}{6}. \tag{A12}$$

References

Bayly, M.B., 1974. An energy calculation regarding the roundness of folds. Tectonophysics 24, 291–316.

Blenkinsop, T., 2000. Deformation Microstructures and Mechanisms in Minerals and Rocks. Kluwer Academic Publishers.

Carter, N.L., Tsenn, M.C., 1987. Flow properties of continental lithosphere. Tectonophysics 136, 27–63.

Cooke, M.L., Mollema, P.N., Pollard, D.D., Aydin, A., 2000. Interlayer Slip and Joint Localization in the East Kaibab Monocline, Utah: Field Evidence and Results From Numerical Modeling. In: Cosgrove, J.W., Ameen, M.S. (Eds.), Forced Folds and Fractures. Geological Society: London. Special Publication, vol. 169, pp. 23–49.

Cooke, M.L., Murphy, S., 2004. Assessing the work budget and efficiency of fault systems using mechanical models. Journal of Geophysical Research 109, B10408.

Craddock, J.P., 1986. Possible thermal controls on thin and thick-skinned faulting, overthrust region: Idaho and Wyoming. Geological Society of America Abstracts with Programs 18, 573.

Dahlen, F.A., Barr, T.D., 1989. Brittle frictional mountain building 1. Deformation and mechanical energy budget. Journal of Geophysical Research 94, 3906–3922.

Dewhurst, D.N., Jones, R.M., 2002. Geomechanical, microstructural, and petrophysical evolution in experimentally reactivated cataclasites: applications to fault-seal prediction. AAPG Bulletin 86, 1383–1405.

DiDonna, B., 2004. Scaling the Buckling Transition of Ridges in Thin Sheets. Ph.D. thesis, University of Chicago.

Dieterich, J.H., 1970. Computer experiments on mechanics of finite amplitude folds. Canadian Journal of Earth Sciences 7, 467–476.

Donath, F.A., Parker, R.D., 1964. Folds and Folding. In: Geological Society of America Bulletin, vol. 75, pp. 45–62.

Elliott, D., 1976a. The motion of thrust sheets. Journal of Geophysical Research 81, 949–963.

Elliott, D., 1976b. Energy balance and deformation mechanisms of thrust sheets. Philosophical transactions of the Royal Society of London. Series A 238, 289–312.

Evans, J.P., 1990. Thickness–displacement relationships for fault zones. Journal of Structural Geology 12, 1061–1065.

Farver, J.R., Yund, R.A., 1991. Measurement of oxygen grain boundary diffusion in natural, fine-grained, quartz aggregates. Geochimica et Cosmochimica Acta 55, 1597–1607.

Fletcher, R.A., 1984. Instability of lithosphere undergoing shortening: a model for Laramide foreland structures. Geological Society of America Abstracts with Programs 16, 83.

Guiton, M.L.E., Leroy, Y.M., Sassi, W., 2003. Activation of diffuse discontinuities and folding of sedimentary layers. Journal of Geophysical Research 108 (B4), 3–20.

Heesakkers, V., Lockner, D., Reches, Z., 2007. The rupture zone of a m2.2 earthquake within the mechanically heterogeneous Pretorius fault-zone, Tautona mine, South Africa (NELSAM project). Geophysical Research Abstracts 9, 05187.

Hunt, G., Muhlhaus, H., Hobbs, B., Ord, A., 1996. Localized folding of visco-elastic layers. Geologische Rundschau 85, 58–64.

Hull, J., 1988. Thickness–displacement relationships for deformation zones. Journal of Structural Geology 10, 431–435.

Ismat, Z., 2006. Cataclastic flow: a means for ensuring ductility within the elastico-frictional regime. Geological Society of America Annual Meeting Abstracts.

Ismat, Z., Mitra, G., 2001a. Folding by cataclastic flow at shallow crustal levels in the Canyon Range, Sevier orogenic belt, west-central Utah. Journal of Structural Geology 23, 355–378.

Ismat, Z., Mitra, G., 2005a. Fold-thrust belt evolution expressed in an internal thrust sheet, Sevier orogeny: the role of cataclastic flow. GSA Bulletin 117, 764–782.

Ismat, Z., Mitra, G., 2005b. Folding by cataclastic flow: evolution of controlling factors during deformation. Journal of Structural Geology 27, 2181–2203.

Ismat, Z., Benford, B., 2007. Deformation in the core of a fold: unraveling the kinematic evolution of tight, multilayer folds developed in the upper crust. Journal of Structural Geology 29, 497–514.

Jeng, F.S., Lin, M.L., Lai, Y.C., Teng, M.H., 2002. Influence of strain rate on buckle folding of an elasto-viscous single layer. Journal of Structural Geology 24, 501–516.

Johnson, A.M., Ellen, S.D., 1974. A theory of concentric, kink, and sinusoidal folding and of monoclinal flexuring of compressible elastic multilayers. Tectonophysics 21, 310–339.

Knipe, R.J., 1989. Deformation mechanisms: recognition from natural tectonites. Journal of Structural Geology 11, 127–146.

Kunzig, R., 2003. Lines of least resistance. Discover Nov., 28–29.

Labotka, T.C., Cole, D.R., Riciputi, L.R., 2000. Diffusion of C and O in calcite at 100 MPa. American Mineralogist 85, 488–494.

Lawton, T.F., Sprinkel, D.F., DeCelles, P.G., Mitra, G., Sussman, A.J., Weiss, M.P., 1997. Sevier Thrust Belt Central-Utah: Sevier Desert to Wasatch Paleau. In: Link, K.P., Kowallis, B.J. (Eds.), BYU Geology Studies Field Trip Guide Book Part II. Geological Society of America Annual Meeting, pp. 33–68.

Lister, G.S., Paterson, M.S., Hobbs, B.E., 1978. The simulation of fabric development in plastic deformation and its application to quartzite: the model. Tectonophysics 44, 107–158.

Lobkovsky, A., Gentges, H.L., Morse, D., Witten, T.A., 1995. Scaling properties of stretching ridges in a crumpled elastic sheet. Science 270, 1482–1485.

Mancktelow, N.S., Abbassi, M.R., 1992. Single layer buckle folding in non-linear materials-II. Comparison between theory and experiment. Journal of Structural Geology 14, 105–120.

Mandl, G., 2000. Faulting in Brittle Rocks: An Introduction to the Mechanics of Tectonic Faults. Springer.

Masek, J.G., Duncan, C.C., 1998. Minimum-work mountain building. Journal of Geophysical Research 103, 907–917.

Matan, K., Williams, R.B., Witten, T.A., Nagel, S.R., 2002. Crumpling a thin sheet. Physical Review Letters 88, 1–4.

McClintock, F.A., Argon, A.S., 1966. Mechanical Behavior of Materials. Addison-Wesley Publishing Company.
Mitra, G., Schmidt, C.J., Chase, R.B., Erslev, E.A., 1993. Deformation Processes in Brittle Deformation Zones in Granitic Basement Rocks: A Case Study from the Torrey Creek Area, Wind River mountains. In: Laramide Basement Deformation in the Rocky Mountain Foreland of the Western United States. Geological Society of America Special Paper, vol. 280, pp. 177–195.
Mitra, G., Boyer, S.E., 1986. Energy balance and deformation mechanisms of duplexes. Journal of Structural Geology 8, 291–304.
Mohamed, Z., Mohamed, K., Gye Chun, C., 2008. Uniaxial compressive strength of composite rock material with respect to shale thickness ratio and moisture content. Electronic Journal of Geotechnical Engineering 13, 1–10.
Ord, A., 1991. Deformation of Rock: A Pressure-Sensitive, Dilatant Material. In: Ord, A., Hobbs, B.E., Muhlhaus, H.B. (Eds.), Localization of Deformation in Rocks and Metals. Pure and Applied Geophysics 137, 337–366.
Passchier, C.W., Trouw, R.A.J., 1996. Microtectonics. Springer-Verlag, Berlin.
Paterson, M.S., 1978. Experimental Rock Deformation – The Brittle Field. Springer-Verlag.
Patton, R.L., Watkinson, A.J., 2005. A viscoelastic strain energy principle expressed in fold-thrust belts and other compressional regimes. Journal of Structural Geology 27, 1143–1154.
Ramberg, H., 1964. Selective buckling of composite layers with contrasted rheological properties; a theory for simultaneous formation of several orders of folds. Tectonophysics 1, 307–341.
Ramsay, J.G., 1974. Development of Chevron Folds. In: Geological Society of America Bulletin, vol. 85 1741–1754.
Reches, Z., 1978a. Analysis of faulting in three-dimensional strain field. Tectonophysics 47, 109–129.
Reches, Z., 1983. Faulting of rocks in three-dimensional strain fields: II. Theoretical analysis. Tectonophysics 95, 133–156.
Reed-Hill, R.E., 1973. Physical Metallurgy Principles. PWS Engineering, Boston.
Rutter, E.H., 1976. The kinetics of rock deformation by pressure solution. Philosophical Transactions of the Royal Society of London, Series A: Mathemetical and Physical Sciences 283, 203–219.
Scholz, C.H., 2002. The Mechanics of Earthquakes and Faulting. Cambridge University Press.
Summers, J.M., 1979. An Experimental and Theoretical Investigation of Multilayer Fold Development. Ph.D. thesis, University of London.
Treagus, S.H., 1988. Strain refraction in layered systems. Journal of Structural Geology 10, 517–527.
Treagus, S.H., 1993. Flow variations in power-law multilayers: implications for competence contrast in rocks. Journal of Structural Geology 15, 423–434.
Twiss, R.J., Moores, E.M., 1992. Structural Geology. W.H. Freeman and Company.
Williams, J.R., 1980. Similar and chevron folds in multilayers, using finite element and geometric models. Tectonophysics 65, 323–338.
Zhang, Y., Hobbs, B.E., Ord, A., Muhlhaus, H.B., 1996. Computer simulation of single layer buckling. Journal of Structural Geology 18, 643–655.